LUND UNIVERSITY

Particle Filter Framework for 6D Seam Tracking Under Large External Forces Using 2D Laser Sensors

Bagge Carlson, Fredrik; Karlsson, Martin; Robertsson, Anders; Johansson, Rolf

Link to publication

Particle Filter Framework for 6D Seam Tracking Under Large External Forces Using 2D Laser Sensors

Fredrik Bagge Carlson*   Martin Karlsson   Anders Robertsson   Rolf Johansson

Abstract— **We outline the development of a framework for 6 DOF pose estimation in seam-tracking applications using particle filtering. The particle filter algorithm developed incorporates measurements from both a 2 DOF laser seam tracker and the robot forward kinematics under an assumed external force. Special attention is paid to modeling of disturbances in the respective measurements, and methods are developed to assist the selection of sensor configurations for optimal estimation performance.**

I. Introduction

Friction stir welding (FSW) is becoming an increasingly popular joining technique that is capable of producing stronger joints than fusion welding, allowing for a reduction of material thickness and weight of the welded components. Conventional, custom-made FSW machines of gantry type are built to support the large forces inherent in the FSW process. The high stiffness required has resulted in expensive and inflexible machinery which has limited the number of feasible applications of FSW as well as the adaptation of FSW as a joining technique. Recently, the use of robotic manipulators in FSW applications has gained significant interest due to the lower cost compared to conventional FSW machinery as well as the much increased flexibility of an articulated manipulator [1], [2]. The downsides of the use of robots include the comparatively low stiffness which causes significant deflections during welding, with a lower quality weld as result.

A typical approach adopted to reduce the uncertainty introduced by deflections is stiffness/compliance modeling [1], [2], [3], [4]. This amounts to finding models of the joint deflections Δq or of the Cartesian deflections Δx on one of the forms

$$\Delta q = C_j(\tau) \tag{1}$$
$$\Delta x = C_C(f) \tag{2}$$

where τ and f are the joint torques and external forces respectively, x is some notion of Cartesian pose, C denotes some, possibly non-linear, compliance function. The corresponding inverse relations are typically referred to as stiffness models. Robotic compliance modeling has been investigated by many authors, where the most straightforward approach is based on linear models obtained by measuring the deflections under application of known external loads. To avoid the dependence on expensive equipment capable of accurately measuring the deflections, techniques such as the clamping method have been proposed [3], [5], [6] for the identification of models on the form (1). This approach makes the assumption that deflections only occur in the joints, in the direction of movement. Hence, deflections are not captured if they occur in the links, or in the joints orthogonally to the movement, limiting the resulting accuracy of the model obtained [5]. In [2], the use of arm-side encoders was investigated to allow for direct measurement of the joint deflections. As of today, arm-side encoders are not available in the vast majority of robots, and the modification required to install them is yet another obstacle to the adaptation of robotic FSW. The method further suffers from the lack of modeling of link- and orthogonal joint deflections.

Cartesian models like (2) have been investigated in the FSW context by [1], [2], [7]. The proposed Cartesian deflection models are local in nature and not valid globally. This requires separate models to be estimated throughout the workspace, which is time consuming and limits the flexibility of the setup.

Although the use of compliance models leads to a reduction of the uncertainty introduced by external forces, it is difficult to obtain compliance models accurate enough throughout the entire workspace. This fact serves as the motivation for complementing the compliance modeling with sensor-based feedback. Sensor-based feedback is standard in conventional robotic arc and spot welding, where the crucial task of the feedback action is to align the weld torch with the seam along the transversal direction, the major uncertainty being the placement of the work pieces. During FSW, however, the uncertainties in the robot pose are significant, while the tilt angle of the tool in addition to its position is of great importance [8]. This requires a state estimator capable of estimating accurately at least four DOF, with slightly lower performance required in the tool rotation axis and the translation along the weld seam. Conventional seam-tracking sensors are capable of measuring 1-3 DOF only [9], [10], limiting the information available to a state estimator and thus maintaining the need for, e.g., compliance modeling.

Motivated by the concerns raised above, we develop a framework for simulation of robotic seam tracking under the influence of large external process forces. We initially develop a particle-filter based state estimation algorithm in Sec. II, capable of incorporating compliance models and sensor-based feedback in order to estimate the full 6 DOF pose of the robot relative to the seam. We then proceed to develop a framework for seam-tracking simulation in Sec. III, where the relation between error sources and estimation performance is analyzed. The framework is further intended to assist the user in selection of an optimal sensor configuration for a given seam, where sensor configurations vary in, e.g., the number of sensors applied and their distance from the tool center point (TCP).

II. METHOD

Initially, a description of how the particle filter's ability to handle non-linear, non-Gaussian systems will be leveraged to estimate the current tool pose relative to the weld seam. The probability densities used in the state transition and measurement update steps are introduced and practical implementation details are described.

A natural state to consider in robotics is the set of joint angles, q, and their velocities, $\dot{q}$. Due to potential deflections in the kinematic structure, the joint angles are not an accurate description of the robot pose in this application. The developed state estimator will therefore work in the space $SE(3)$, represented as 4×4 transformation matrices, which further allows for a natural inclusion of sensor measurements. The sensor information available from the robot is naturally transformed to $SE(3)$ by means of the forward kinematics function $F_k(q)$. Due to the typically low velocities and accelerations present during FSW, we chose to not include velocities in the state to be estimated. This will reduce the state dimension and computational burden significantly, while maintaining a high estimation performance.

A. Preliminaries

This section briefly introduces a number of coordinate frames and variables used in the later description of the method. For a general treatment of coordinate frames and transformations, see [11].

Table I lists all coordinate frames that will be used to describe poses, see Fig. 1 for reference, and all variables referred to in the following description. All Cartesian-space variables are given in the frame $\mathcal{RB}$ unless otherwise noted.

B. Particle filter

A brief description of the well known particle filter (PF) is given. For a thorough introduction, please refer to one of many texts on the subject [12], [13], [14].

For a linear, Gaussian system, the filtering densities at each sample instant are available in closed form through the Kalman filter (KF) [15]. In the non-linear, non-Gaussian case, computing the exact filtering density is
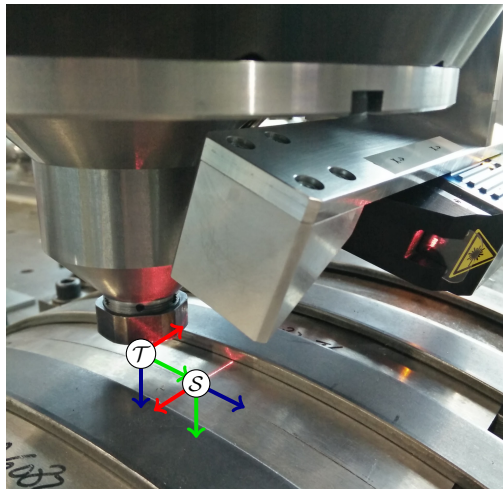

Fig. 1. Coordinate frames $(x, y, z) = $ (red, green, blue). The origin of frame $\mathcal{S}$ is located in the laser plane at the desired seam intersection point.

TABLE I
DEFINITION AND DESCRIPTION OF FRAMES AND VARIABLES.

$\mathcal{RB}$		Robot base frame.
$\mathcal{T}$		Tool frame, attached to the (TCP).
$\mathcal{S}$		Sensor frame, specified according to Fig. 1.

Variable		Description
q	$\in \mathbb{R}^n$	Joint Coordinate
$\dot{q}$	$\in \mathbb{R}^n$	Joint velocity
x	$\in SE(3)$	Tool pose (State)
τ	$\in \mathbb{R}^n$	Joint torque
f	$\in \mathbb{R}^6$	External force/torque
m	$\in \mathbb{R}^2$	Laser measurement in $\mathcal{S}$
m_a	$\in \mathbb{R}^1$	Laser angle measurement in $\mathcal{S}$
e	$\in \mathbb{R}^2$	Measurement error
T_A^B	$\in SE(3)$	Transformation matrix from $\mathcal{B}$ to $\mathcal{A}$
$F_k(q)$	$\in SE(3)$	Robot forward kinematics at pos. q
$J(q)$	$\in \mathbb{R}^{6 \times n}$	Manipulator Jacobian at pos. q
$\hat{a}$		Estimate of variable a
a^+		a at the next sample instant
$\bar{a}$		Reference for variable a
$a_{i:j}$		Elements $i, i+1, ..., j$ of a
$\langle T \rangle$	$\in \mathbb{R}^6$	The twist coordinate representation of T

no longer tractable. The PF resolves this problem by approximating the filtering densities by a collection of samples (particles), also referred to as state hypotheses. Each iteration of the filter algorithm amounts to propagating the particles forward in time using a state transition density $p(x^+|x)$. This density incorporates the uncertainty present in the state transition similar to the state transition noise in the KF. However, for the PF, the state noise is not restricted to be Gaussian. The mean of $p(x^+|x)$ can be any arbitrary non-linear function of the current state, control signals etc..

When a measurement is available, each particle is assigned a weight based on the likelihood of the measurement, given the state of the particle, using the sensor measurement density $p(m|x)$ and the robot measurement density $p(q, f|x)$.

To avoid using the finite collection of particles to

explore parts of the state space with a small posterior probability, particles may be re-sampled with a probability of surviving to the next iteration proportional to their weight.

A simple PF algorithm is given in Algorithm 1.

Algorithm 1 A simple particle filter algorithm.

Initialize particles using a prior distribution;
repeat
    Assign weights to particles using $p(m|x)$ and $p(q, f|x)$;
    Calculate a state estimate based on the weighted collection of particles;
    Re-sample particles based on weights;
    Propagate particles forward using $p(x^+|x, \dot{f})$;
until Done

C. Densities

This section introduces and motivates the various densities used in the particle filter.

1) State transition:

$$p(x^+|x, \dot{f}) \tag{3}$$

The mean of the state transition density (3) is given by the robot reference trajectory. Denote by T^+ the incremental transformation from $F_k(\bar{q})$ to $F_k(\bar{q}^+)$ such that

$$F_k(\bar{q}^+) = T^+ F_k(\bar{q})$$

The mean of the state transition density is thus

$$\mu\left\{p(x^+|x, \dot{f})\right\} = T^+ = F_k(\bar{q}^+)\, F_k(\bar{q})^{-1}$$

The shape of the density should encode the uncertainty in the update of the robot state from one sample to another. For a robot moving in free space, this uncertainty is usually small. Under the influence of varying external process forces, however, significant uncertainty is introduced. Based on this assumption, the width of the density can be chosen as a function of the process force.

2) Robot measurement update:

$$p(q, f|x) \tag{4}$$

The mean of the robot measurement density (4) is given by the robot internal sensors and forward kinematics according to

$$\mu\left\{p(q, f|x)\right\} = F_k(q + C_j(\tau)) \tag{5}$$

where $C_j(\tau)$, if available, is a model of deflections caused by large process forces [3], [5], [6].

The uncertainty in the robot measurement comes from several sources. The joint resolvers/encoders are affected by noise, which is well modeled as a Gaussian random variable. When Gaussian errors, e_q, in the joint measurements are propagated through the linearized FK, the covariance matrix Σ_C of the resulting Cartesian-space errors e_C is obtained by approximating $e_q = dq$ as

$$q_m = q + e_q = q + dq$$
$$e_q \sim \mathcal{N}(0, \Sigma_q)$$
$$e_C \sim \mathcal{N}(0, J\Sigma_q J^\top)$$

where q_m is the measured value. The Cartesian covariance matrix is given by

$$e_C = \frac{d\langle F_k(q)\rangle}{dq} dq = J\, dq = J\, e_q$$
$$\Sigma_C = \mathbb{E}\left\{e_C\, e_C^\top\right\} = \mathbb{E}\left\{J\, e_q\, e_q^\top J^\top\right\} = J\, \mathbb{E}\left\{e_q\, e_q^\top\right\} J^\top$$

where the approximation $J(q + e_q) \approx J(q)$ has been made. The twist coordinate representation $\langle F_k(q)\rangle$ is obtained by taking the logarithm of the transformation matrix $\log(F_k(q))$, which produces a twist $\xi \in se(3)$, and the operation $\xi^\vee \in \mathbb{R}^6$ returns the twist coordinates [11]. The discussion on the errors associated with the robot measurements are treated in more detail in Sec. IV. Except for the measurement noise, the errors in the robot measurement update density are not independent between samples. The error in both the forward kinematics and the compliance model is configuration dependent and thus highly correlated in time due to bounded velocity of the robot leading to slow changes in the configuration. The standard derivation of the particle filter relies on the assumption that the measurement errors constitute a sequence of independent, identically distributed (i.i.d.) random variables. Independent measurement errors can be averaged between samples to obtain a more accurate estimate, which is no longer possible with correlated errors where several consecutive measurements all suffer from the same error.

Time-correlated errors are in general hard to handle in the particle filtering framework and no systematic way to cope with this problem has been found. One approach is to incorporate the correlated error as a state to be estimated [16], [17]. This is feasible only if there exist a way to differentiate between the different sources of error. State augmentation further doubles the state dimension, with a corresponding increase in computational complexity.

Since only a combination of the tracking error, the kinematic error and the dynamic error is measurable, we propose to model the time-correlated uncertainties as a uniform random variable with a width d chosen as the maximum expected error. When performing the measurement update with the densities of several perfectly correlated uniform random variables, the posterior distribution equals the prior distribution. The distribution is thus invariant under self fusion. See Fig. 2 for an illustration.

The complete robot measurement density, Eq. (4), is formed by the convolution of the densities for a Gaussian,
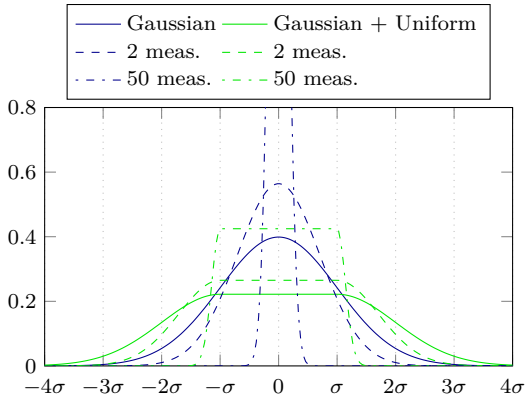
Fig. 2. Illustration of measurement densities and the posterior densities after several performed measurement updates, for $d = \sigma$.

Fig. 3. Illustration the multivariate version of the robot measurement density, Eq. (8).

p_G, and a uniform, p_U, random variable, according to

$$p(q, f|x) = \int_{\mathbb{R}^k} p_U(x - y) \, p_G(y) \, dy \qquad (6)$$

where k is the dimensionality of the state x. This integral has no closed form solution, but can be evaluated numerically. Instead of evaluating Eq. (6), which is computationally expensive and must be done for every particle at every time step, we propose the following approximation

$$p(q, f|x) \approx \begin{cases} C & \text{if } |\Delta x| \le d \\ C \exp\left(-\frac{(|\Delta x| - d)^2}{2\sigma^2}\right) & \text{if } |\Delta x| > d \end{cases} \qquad (7)$$

with Δx taken to be the element-wise difference between the positional coordinates of x and a mean vector $\mu \in \mathbb{R}^3$, $\Delta x = x - \mu$, and the normalization constant

$$C = \frac{1}{\sqrt{2\pi}\sigma + 2d}$$

This approximation reduces to the Gaussian distribution if the width of the uniform part $d = 0$, and to the uniform distribution as $\sigma \to 0$. Equation (7) is given for the one-dimensional case, one possible extension to higher dimensions is given by

$$p(q, f|x) = \begin{cases} D & \text{if } \left\|\Delta x\right\|_2 \le d \\ D \exp\left(-\frac{1}{2}\delta x^\top \Sigma^{-1} \delta x\right) & \text{if } \left\|\Delta x\right\|_2 > d \end{cases} \qquad (8)$$

$$\delta x = \left(1 - \frac{d}{\left\|\Delta x\right\|_2}\right) \Delta x$$

$$D = \frac{1}{(2\pi)^{\frac{k}{2}} \sqrt{\det(\Sigma)} + V(d, k)}$$

where k is the state dimension and $V(d, k)$ is the volume of a k-dimensional sphere with radius d.

The univariate distribution, and the distribution of several fused measurements, is shown in Fig. 2. An illustration of the multivariate case with

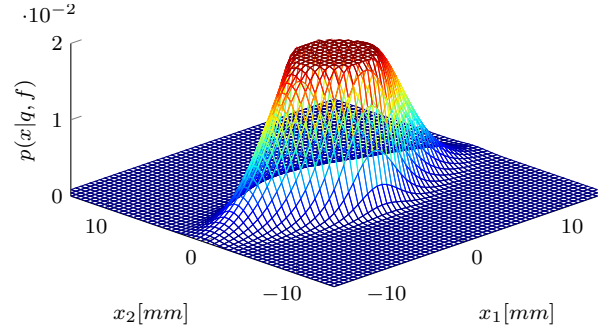$$\Sigma = \begin{bmatrix} 4 & 0 \\ 0 & 1 \end{bmatrix}, \quad d = 3$$

is shown in Fig. 3.

The width of the uniform random variable $d = d(f)$ is chosen as a function of the process force

$$d(f) = d_0 + k_d \left\|f\right\|$$

where d_0 is chosen with respect to the maximum absolute positioning error of the robot in the relevant work-space volume and $k_d \left\|f\right\|$ reflects the increase in uncertainty with the magnitude of the process force.

3) Laser sensor measurement update:

$$p(m|x)$$

Evaluating the laser measurement density is less straightforward. Given a state hypothesis $\hat{x}$, a seam location hypothesis $\hat{m}$ is calculated using T_T^S according to

$$\hat{m} = (\hat{x}T_T^S)_{1:3,4} + [m^\top \; 0]^\top \qquad (9)$$

To evaluate the distance e between $\hat{m}$ and the nominal trajectory, a search for the closest nominal trajectory points is performed. The error e is then calculated as the distance between $\hat{m}$ and the intersection point p_i between the laser plane and the line v between the closest seam point on each side on the laser plane, refer to Fig. 4 for an illustration. The intersection point p_i must satisfy the following two equations

$$\left.\begin{array}{c} p_i = p_1 + \gamma v \\ 0 = n^\top (p_i - \hat{m}) \end{array}\right\} \Rightarrow \gamma = \frac{n^\top (\hat{m} - p_1)}{n^\top v}$$

where n is the normal of the laser light plane.

The mean of $p(m|x)$ is thus equal to

$$\mu\{p(m|x)\} = p_i$$

and the shape should be chosen as the error distribution of the laser sensor, here modeled as a normal distribution according to

$$p(m|x) = (2\pi)^{-\frac{3}{2}}|\Sigma|^{-\frac{1}{2}} \exp\left(-\frac{1}{2}e^\top \Sigma^{-1} e\right), \quad e = \hat{m} - p_i$$

Many seam-tracking sensors are capable of measuring also the angle around the normal of the laser plane. An angle measurement, m_a, is easily compared to the
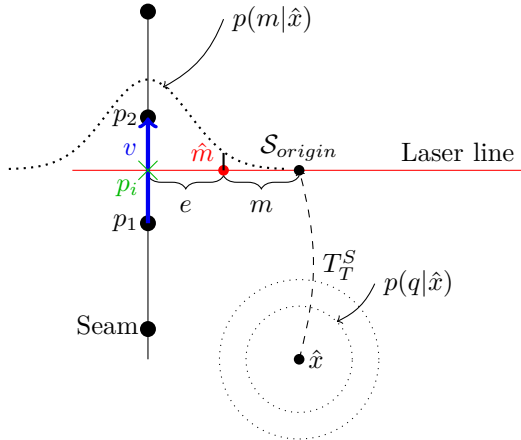
Fig. 4. Illustration of the relations between a particle $\hat{x}$ (TCP hypothesis), its belief of the location of the laser line and the laser measurement m (Eq. (9)). Particles for which the distance, e, between the measurement hypothesis $\hat{m}$ and the seam intersection point p_i is small, in terms of the distribution $p(m|x)$, are more likely to be correct estimates of the current state x.

corresponding angle hypothesis of a particle using standard roll, pitch, yaw calculations. Using the convention in Fig. 1, the angle around the normal of the laser plane corresponds to the yaw angle. Roll and pitch angles are not directly measurable by this type of sensor. Using a sensor with two or more laser planes, it is possible to estimate the full orientation of the sensor. This will be analyzed further in Sec. III.

D. Nominal trajectory

To get a suitable representation of the nominal trajectory used to propagate the particles forward, a simulation of the robot program is performed using a simulation software, often provided by the robot manufacturer. This procedure eliminates the need to reverse engineer the robot path planner. During the simulation, a stream of joint angles is saved which, when run through the forward kinematics, returns the nominal trajectory in Cartesian space. Methods for generating a nominal trajectory for simulation experiments are provided in the simulation framework.

E. Reduction of computational time

Since the intersection point between the nominal seam line and the laser light plane is calculated, a reduction of the number of points to traverse in the trajectory search can be achieved by approximating the trajectory with a piece-wise affine function. To this end, we solve the following convex optimization problem,

$$
\begin{aligned}
\underset{z,w}{\text{minimize}} \quad & \|y - z\|_F^2 + \lambda \sum_{i=1}^{N-2} \sum_{j=1}^{3} |w_{i,j}| \\
\text{subject to} \quad & \|y - z\|_\infty \leq \epsilon \\
& w_{i,j} = z_{i,j} - 2z_{i+1,j} + z_{i+2,j}
\end{aligned}
\tag{10}
$$

where $y \in \mathbb{R}^{N \times 3}$ are the positions of the nominal trajectory points, z is the approximation of y, and
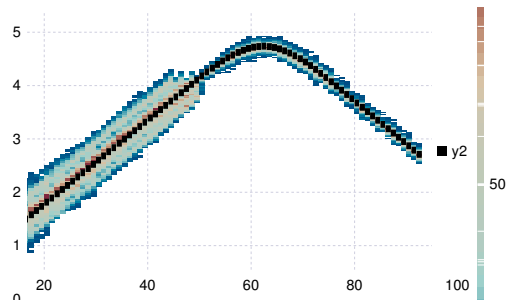

Fig. 5. Visualization of the particle distributions during a simulation. The black line indicates one coordinate of the true state as a function of the time step and the heatmap illustrates the density of the particles. This figure illustrates how the uncertainty of the estimate is reduced as one sensor approaches a feature in the trajectory. The feature is in this case a sharp bend in the otherwise straight seam.

ϵ is the maximum allowed approximation error. The non-zero elements of w will determine the location of the knots in the piece-wise affine approximation and λ will influence the number of knots.[1] The proposed optimization problem does not incorporate constraints on the orientation. The orientation approximation error will however be small if we assume differentiability and bounded curvature of the trajectory and constrain the translational approximation to be small, as in Eq. (10). For an introduction to convex optimization, see [18] and for an overview of trend filtering problems like (10) see [19].

III. Simulation framework

A. Visualization

An often time-consuming part during the implementation of a particle filtering framework is the tuning of the filter parameters. Due to the highly nonlinear nature of the present filtering problem, this is not as straightforward as in the Kalman-filtering scenario.

To assist in the tuning of the filter, we provide a visualization tool that displays the true trajectory as traversed by the robot together with the distribution of the particles, as well as each particle's hypothesis measurement location. An illustrative example is shown in Fig. 5, where a screen shot of one dimension in the filter state is shown as a function of time.

To further aid the tuning of the filter, we perform several simulations in parallel with randomly perturbed filter parameters and perform statistical significance tests to determine the parameters of most importance to the result for a certain sensor/trajectory configuration. Figure 6 displays the statistical significance of various filter parameters for a certain trajectory and sensor configuration. The color coding indicate the log(P)-values for the corresponding parameters in a linear model predicting the errors in Cartesian directions and orientation. As

---

[1] $w_i = z_i - 2z_{i+1} + z_{i+2}$ is a discrete second order differentiation of z.
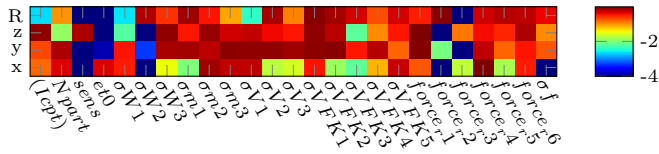
Fig. 6. An illustration of how the various parameters in the software framework can be tuned. By fitting linear models, with tuning parameters as factors, that predict various errors as linear combinations of parameter values, parameters with significant effect on the performance can be identified using the log(P)-values (color coded). The x-axis indicates the factors and the y-axis indicates the predicted errors in orientation and translation. The parameters are described in detail in the software framework.
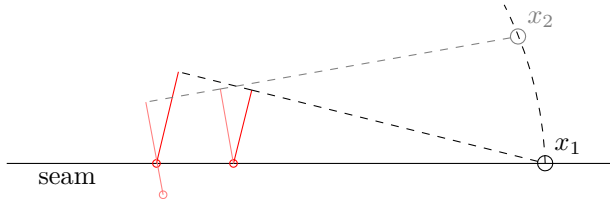

Fig. 7. Illustration of how a sensor with a single laser stripe can not distinguish between wrong translation and wrong orientation. The figure depicts two hypotheses (x_1, x_2), both share the closest measurement point on the seam. The second laser stripe invalidates the erroneous hypothesis x_2 which would have the second measurement point far from the seam.

an example, the figure indicates that the parameter σ_{W2}, corresponding to the orientation noise in the state update, has a significant impact on the errors in all Cartesian directions. The sign and value of the underlying linear model can then serve as a guide to fine tuning of this parameter.

B. Sensor configurations

The optimal sensor configuration depends on the amount of features in the trajectories, where a feature is understood as a localizable detail in the trajectory. The estimation performance is further critically dependent on the number of laser light planes that intersect the seam. A single laser sensor can measure three degrees of freedom, two translations and one orientation. The remaining tree DOFs are in general not observable. This is illustrated in the planar case in Fig. 7. All particles lying on a capsule manifold, generated by the spherical movement around the measurement location, together with a sliding motion along the seam, are equally likely given the measurement. A second measurement eliminates the spherical component of the capsule, leaving only the line corresponding to the sliding motion along the seam unobservable. The unobservable subspace left when two or more laser planes are used can only be reduced by features in the seam, breaking the line symmetry (illustrated in Fig. 5), or the forward kinematics measurement from the robot.

Consider Fig. 8, where the resulting errors for two trajectory types and several sensor configurations (0,1,2 sensors) are displayed. The trajectories referred to in the figure are generated as follows. The xy-trajectory
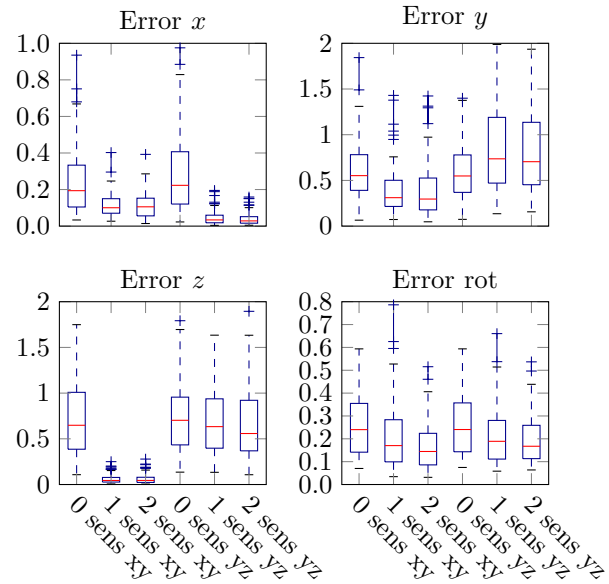

Fig. 8. Error distributions for various sensor configurations (0-2 sensors) and two different trajectory types (xy,yz). In both trajectory cases, y is the major movement direction along which the laser sensors obtain little or no information. The same filter parameters, tuned for the xy-trajectory, were used in all experiments.
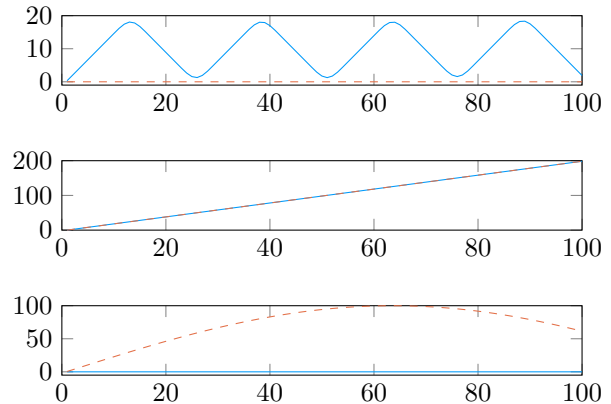

Fig. 9. Trajectories xy (blue solid) and yz (orange dashed). Distance [mm] along each axis (x, y, z) is depicted as a function of time step.

lies entirely in the xy-plane of the tool frame $\mathcal{T}$, with a linear movement of 200 mm in the y-direction and a smooth, 20 mm amplitude, triangle-wave motion in the x-direction. The yz-trajectory lies in the yz-plane, with a linear movement of 200 mm in the y-direction and a 100 mm amplitude, sinusoidal, motion in the z-direction. The trajectories are depicted in Fig. 9. It is clear that the type of trajectory is important for the resulting estimation error, in this case, the filter was tuned for trajectory type xy. Figure 8 illustrates the difficulties in determining the translation along the direction of movement when no features are present, as well as the benefit of sensor feedback in the measurable dimensions. The provided visualization tools assist in re-tuning the filter for a new trajectory, and can suggest optimal configurations of the available seam-tracking sensors.

IV. Discussion

The kinematic model of the robot used in the forward kinematics calculations is often inaccurate, and errors in the absolute positioning accuracy of an industrial robot can often be in the order of 1 mm or more [20], [21]. To characterize this uncertainty without performing a full kinematic calibration is usually hard, since it is a non-linear function of the errors in link-lengths, offsets etc. in the kinematic model. Possibilities include modeling this uncertainty as a Gaussian distribution with a variance corresponding to the average error in the considered work space volume, or as a uniform distribution with a width corresponding to the maximum error. These figures are usually provided by the robot manufacturer, or can be obtained using, e.g., an external optical tracking system.

A third source of uncertainty is compliance in the structure of the robot. Deflections in the robot joints and links caused by large process forces result in an uncertainty in the measured tool position. This problem can be mitigated by a compliance model, $C_j(\tau)$ in Eq. (5), reducing the uncertainty to the level of the model uncertainty [3].

V. Conclusions

We have suggested a particle-filter based state estimator capable of estimating the full 6 DOF pose of the tool relative to the seam in a seam-tracking scenario. Sensor fusion is carried out between the robot internal measurements, propagated through a forward kinematics model with large uncertainties due to the applied process forces, and measurements from a class of seam-tracking laser sensors. We have highlighted some of the difficulties related to state estimation where accurate measurements come in a reduced dimensional space, together with highly uncertain measurements of the full state space, where the uncertainties are highly correlated in time.

References

[1] J. De Backer, "Feedback control of robotic friction stir welding," Ph.D. dissertation, ISBN 978-91-87531-00-2, University West, Trollhättan, Sweden, 2014.

[2] M. Guillo and L. Dubourg, "Impact & improvement of tool deviation in friction stir welding: Weld quality & real-time compensation on an industrial robot," *Robotics and Computer-Integrated Manufacturing*, vol. 39, pp. 22–31, 2016.

[3] C. Lehmann, B. Olofsson, K. Nilsson, M. Halbauer, M. Haage, A. Robertsson, O. Sörnmo, and U. Berger, "Robot joint modeling and parameter identification using the clamping method," 2013, pp. 843–848.

[4] J. De Backer and G. Bolmsjö, "Deflection model for robotic friction stir welding," *Industrial Robot: An International Journal*, vol. 41, no. 4, pp. 365–372, 2014.

[5] O. Sörnmo, "Adaptation and learning for manipulators and machining," Ph.D. dissertation, ISRN TFRT--1110--SE, Lund University, Lund, Sweden, 2015.

[6] B. Olofsson, "Topics in machining with industrial robot manipulators and optimal motion control," Ph.D. dissertation, ISRN TFRT--1108--SE, Lund University, Lund, Sweden, 2015.

[7] E. Abele, S. Rothenbücher, and M. Weigold, "Cartesian compliance model for industrial robots using virtual joints," *Production Engineering*, vol. 2, no. 3, pp. 339–343, 2008.

[8] J. De Backer, A.-K. Christiansson, J. Oqueka, and G. Bolmsjö, "Investigation of path compensation methods for robotic friction stir welding," *Industrial Robot: An International Journal*, vol. 39, no. 6, pp. 601–608, 2012.

[9] N. R. Nayak and A. Ray, *Intelligent seam tracking for robotic welding*. Springer Science & Business Media, London, UK, 2013.

[10] X. Gao, D. You, and S. Katayama, "Seam tracking monitoring based on adaptive kalman filter embedded elman neural network during high-power fiber laser welding," *Industrial Electronics, IEEE Transactions on*, vol. 59, no. 11, pp. 4315–4325, 2012.

[11] R. M. Murray, Z. Li, and S. S. Sastry, *A mathematical introduction to robotic manipulation*. CRC Press, 1994.

[12] F. Gustafsson, "Particle filter theory and practice with positioning applications," *Aerospace and Electronic Systems Magazine, IEEE*, vol. 25, no. 7, pp. 53–82, 2010.

[13] S. Thrun, W. Burgard, and D. Fox, *Probabilistic Robotics*, ser. Intelligent robotics and autonomous agents. MIT Press, Cambridge, Massachusetts, 2005.

[14] J. Rawlings and D. Mayne, *Model Predictive Control: Theory and Design*. Nob Hill Pub. Madison, Wisconsin, 2009.

[15] R. E. Kalman, "A new approach to linear filtering and prediction problems," *J. Basic Engineering*, vol. 82, no. 1, pp. 35–45, 1960.

[16] G. Evensen, "The ensemble Kalman filter: theoretical formulation and practical implementation," *Ocean Dynamics*, vol. 53, no. 4, pp. 343–367, 2003.

[17] K. Åström and B. Wittenmark, *Computer-Controlled Systems: Theory and Design, Third Edition*. Dover Publications, Minola, NY, 2013.

[18] S. Boyd and L. Vandenberghe, *Convex optimization*. Cambridge University Press, Cambridge, UK, 2004.

[19] R. J. Tibshirani, "Adaptive piecewise polynomial estimation via trend filtering," *The Annals of Statistics*, vol. 42, no. 1, pp. 285–323, 2014.

[20] B. Mooring, Z. Roth, and M. Driels, *Fundamentals of manipulator calibration*. J. Wiley, New York, 1991.

[21] A. Nubiola and I. A. Bonev, "Absolute calibration of an ABB IRB 1600 robot using a laser tracker," *Robotics and Computer-Integrated Manufacturing*, vol. 29, no. 1, pp. 236 – 245, 2013.